Rare Met. (2022) 41(9):3170–3179
https://doi.org/10.1007/s12598-022-02039-5

RARE METALS

ORIGINAL ARTICLE

# Enhanced ethanol oxidation over Pd nanoparticles supported porous graphene-doped MXene using polystyrene particles as sacrificial templates

**Yi-Zhe Chen, Ming Zhou, Yu-Fu Huang, Yan-Yun Ma*, Luo-Yi Yan, Xin-Wen Zhou, Xin-Zhou Ma, Xue-Ling Zhao, Cheng Chen, Juan Bai, Dong-Hai Lin***

Received: 20 January 2022 / Revised: 15 February 2022 / Accepted: 20 February 2022 / Published online: 30 June 2022


**Abstract** Fabrication of superior catalytic performance palladium-based catalysts with affordable cost is the key to develop direct ethanol fuel cell. Herein, Pd-decorated three-dimensional (3D) porous constructed from graphene oxide (GO) and MXene combining with polystyrene (PS) particles as sacrificial templates (Pd/GO-MXene-PS) to elevate the catalytic performance for ethanol oxidation was proposed. The 3D porous interconnected structure of Pd/GO-MXene-PS was characterized by scanning electron microscope (SEM), transmission electron microscope (TEM) and Brunner−Emmet−Teller (BET). By optimizing the doping ratio of MXene to GO, the mass activity of Pd/$GO_5$-$MXene_5$-PS (2944.0 mA·$mg^{-1}$) was 3.0 times higher than that of commercial Pd/C (950.4 mA·$mg^{-1}$) toward ethanol oxidation in base solution. Meanwhile, the rotating disk electrode (RDE) results demonstrated that Pd/$GO_5$-$MXene_5$-PS had a faster kinetics of ethanol oxidation. The enhanced ethanol oxidation over Pd/$GO_5$-$MXene_5$-PS could attribute to the excellent 3D interconnected porous structure, large surface area, good conductivity and homogeneous Pd distribution. This work provided a new idea for creating 3D porous MXene composite materials in electrocatalysis.

**Keywords** Pd nanoparticles; Ethanol oxidation; Graphene; MXene; Polystyrene (PS) template; Rotating disk electrode (RDE)

**Supplementary Information** The online version contains supplementary material available at https://doi.org/10.1007/s12598-022-02039-5.

Y.-Z. Chen, M. Zhou, Y.-F. Huang, X.-L. Zhao, C. Chen, J. Bai, D.-H. Lin*
Shanghai Engineering Research Center of Advanced Thermal Functional Materials, Shanghai Key Laboratory of Engineering Materials Application and Evaluation, School of Energy and Materials, Shanghai Polytechnic University, Shanghai 201209, China
e-mail: dhlin@sspu.edu.cn

Y.-Y. Ma*
Institute of Functional Nano & Soft Materials (FUNSOM), Jiangsu Key Laboratory for Carbon-Based Functional Materials & Devices, Soochow University, Suzhou 215123, China
e-mail: mayanyun@suda.edu.cn

L.-Y. Yan, X.-W. Zhou
College of Biological and Pharmaceutical Sciences, China Three Gorges University, Yichang 443002, China

X.-Z. Ma
School of Materials Science and Hydrogen Energy, Foshan University, Foshan 528000, China

J. Bai
School of Chemistry and Physics, Queensland University of Technology, Brisbane, QLD 4000, Australia

## 1 Introduction

As a result of the extensive use of conventional fossil energy sources, the concentration of carbon dioxide steadily increases, leading to climate change and environmental pollution problems [1, 2]. Direct ethanol fuel cell (DEFC) has been extensively studied due to its environmental friendliness, high stability and other advantages [3–5]. Despite palladium-based catalysts have unique innate advantages under alkaline conditions, their low energy conversion efficiency limits their commercial applications [6, 7]. Carbon materials (such as graphene [8, 9], carbon nanotubes [10, 11], mesoporous carbon [12, 13] and carbon nanofibers [14]) have been used as electrocatalyst support for DEFC due to its excellent mass

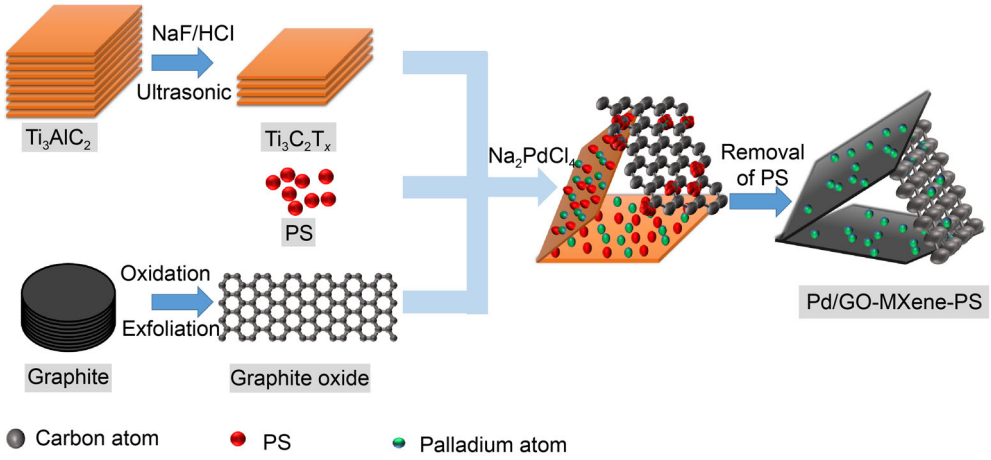


**Scheme 1** Schematic illustration for preparation of 3D Pd/GO-MXene-PS architecture

transfer performance, high specific surface area and excellent structure effect between active components [15, 16]. However, carbon-based catalytic carriers still have some shortcomings, such as low catalytic activity and stability [3]. Therefore, combining carbon with some inorganic materials is a common strategy to adjust the conductivity of the carrier and increase the specific surface area. For example, melamine as a nitrogen source was proposed to produce nitrogen-doped graphene oxide and chosen as the most promising anion exchange membranes candidate for DEFC [17].

MXene materials have the advantages of good hydrophilicity, large specific surface area and excellent electrical conductivity [17, 18]. In addition, MXene materials also provide many functional groups (−F, −OH, −O), which also beneficial for the adsorption of metal ions [19–21]. Unfortunately, the poor surface charge transfer of MXene limits their application [22]. In order to enhance charge transfer, conductive polymers [23], carbon nanotube [24, 25], graphene [26, 27] or metal oxide [28] were mixed with MXene. Three-dimensional (3D) MXene hollow sphere materials with large specific surface area and flexibility are commonly used for supercapacitors. Huang et al. successfully loaded Pt nanoparticles onto graphene oxide (GO)-MXene mixtures [29]. The synthesized catalysts exhibited excellent catalytic activity for methanol oxidation which may be attributed to the optimal structure of GO-MXene carriers and the better adsorption capacity of GO-MXene support with metal NPs. Nevertheless, the fabrication of Pd-decorated three-dimensional porous structure built from GO and MXene combined with polystyrene (PS) particles as sacrificial templates holds enormous promise in the electrocatalysis was rare.

In this work, 3D GO-MXene structure for the catalyst support was synthesized. The unique 3D GO-MXene structure was synthesized from PS spheres, MXene and GO solution and then calcined at 500 °C to remove PS template. Two-dimensional (2D) GO-MXene was transformed into 3D GO-MXene skeleton by sacrificing PS spherical colloidal template, and $Pd^{2+}$ was reduced to Pd nanoparticles by ethanol (shown in Scheme 1). Electrochemical results employed that PS hybrid Pd/GO-MXene-PS material has better catalytic performance toward ethanol oxidation reaction (EOR) than that of Pd/GO-MXene material and commercial Pd/C. Meanwhile, the kinetic process of EOR was investigated by rotating disk electrode (RDE) technique. Pd/GO-MXene-PS possesses the excellent kinetic performance for EOR.

## 2 Experimental

### 2.1 Chemicals and materials

$Ti_3C_2T_x$ (≥ 99 wt%), ethanol (≥ 98 wt%), hydrogen peroxide (30 wt%), palladium chloride ($PdCl_2$, Adamas, Pd > 59 wt%), phosphoric acid (85 wt%), sodium chloride (> 99.5 wt%), potassium permanganate (> 99.99 wt%), sodium fluoride (≥ 98 wt%), sulfuric acid (98 wt%), sodium hydroxide (99 wt%), dimethyl sulfoxide (DMSO), acrylic acid (99 wt%), styrene (99 wt%). hydrochloric acid (37 wt%), graphite powder and commercial Pd/C were got from Alfa Aesar. All other chemicals were of analytical grade and applied as purchased.

### 2.2 Synthesis of $Ti_3C_2T_x$ MXene and GO

MXene was prepared according to the literature with little modification [30]. Typically, 2.0 g of $Ti_3AlC_2$ powder was added to the mix solution, which consisted of 2.0 g NaF, 15 ml hydrochloric acid and 15 ml $H_2O$. The etching solution containing $Ti_3AlC_2$ powder was magnetically

stirred at 60 °C for 48 h. The solution was centrifugally rinsed with deionized (DI) water for several times until pH reached 6 and then rinsed with anhydrous ethanol three times. The powder was stored in a vacuum-dried environment at 60 °C. For intercalation, 0.25 g $Ti_3C_2T_x$ powder was added to 10 ml DMSO and stirred at 25 °C for 18 h. To further achieve stratification, the material was added to 80 ml DI water. Then, in $N_2$ atmosphere, the solution was treated with ultrasound for 8 h. Finally, the mixed solution was centrifuged at 4000 r·min$^{-1}$ 2 h to obtain the final material.

### 2.3 Synthesis of Pd/GO-MXene-PS

PS spheres were synthesized by a slightly modified microemulsion polymerization approach without surfactant [31]. GO was obtained using the improved Hummer method with little modification [32]. For Pd/GO-MXene-PS, PS dispersion (32.1 mg·ml$^{-1}$, 0.312 ml) was added to 0.688 ml DI water, and ultrasonic treated for 30 min to form the homogeneous solution. Then, MXene (5 ml, 2 mg·ml$^{-1}$) and GO (5 ml, 2 mg·ml$^{-1}$) dispersions were added to PS dispersions drop by drop, and ultrasound for 20 min to prepare GO-MXene-PS. Then, $Na_2PdCl_4$ (4 ml, 20 mmol·L$^{-1}$) solution was added slowly to the mixture. Add 40 ml anhydrous ethanol and stir the mixture in an oil bath at 120 °C for 4 h. Finally, the samples were centrifuged, washed and dried to produce solid powder. Catalysts with volume ratios of 10:0, 7:3, 5:5, 3:7 and 0:10 were prepared according to the volume ratios of GO solution and MXene solution. They were named as Pd/$GO_{10}$-$MXene_0$-PS, Pd/$GO_7$-$MXene_3$-PS, Pd/$GO_5$-$MXene_5$-PS, Pd/$GO_3$-$MXene_7$-PS, Pd/$GO_0$-$MXene_{10}$-PS, respectively. In order to investigate the optimal thermal decomposition temperature of PS, we performed TGA tests on the catalyst before calcination (Fig. S1). The results showed that the thermal decomposition of PS occurred in the interval of 300 to 450 °C. Therefore, in order to completely remove PS, the above solids were calcined in $N_2$ atmosphere at 500 °C for 1 h (denoted as Pd/GO-MXene-PS). Pd/$GO_5$-$MXene_5$ was prepared by the same method except without PS.

### 2.4 Characterization

X-ray powder diffractometer (XRD) was analyzed by an D8-advance instrument (Bruker). X-ray photoelectron spectroscopy (XPS, Escalab 250XI, Thermo Scientific, UK) was applied to determine the elemental composition of samples before and after deposition. The morphological characteristics and specific surface area of the samples were tested by transmission electron microscopy (TEM, FEI Tenai F20, FEI, USA), scanning electron microscopy (SEM, S-4800, Hitachi, Japan) and Brunner−Emmet−Teller measurements (BET, 2020 HD88, USA). The chemical structure of the catalysts was analyzed by using a Raman spectrometer (Senterra, Karlsruhe, Germany). The electrochemical experiment was tested by chronoamperometry and cyclic voltammetry (CV) at the electrochemical workstation (CHI760E, Chenhua, China). The inductively coupled plasma-optical emission spectroscopy (ICP-OES, ICAP 7000, Thermo Scientific) was used to analyze the loading of Pd in the catalyst. Probing the optimal thermal decomposition temperature of PS by using a thermogravimetric analyzer (TGA, STA-449, Germany).

### 2.5 Electrochemical experiment

The electrochemical detection of the catalyst was characterized in the common three-electrode cell at 25 °C. The reference electrode was silver chloride electrode (Ag/AgCl), and Pt flake was used as the counter electrode. After polishing with 0.3 and 0.05 μm alumina powders, ultrasonic treatment was conducted in nitric acid/water (*V*/*V* = 1:1), ethanol and DI for glassy carbon (GC) electrode 5 min, respectively. 5.0 mg Pd/GO-MXene-PS composite was added to a mixed solution of 700 μl ethanol, 260 μl Millipore water and 40 μl Nafion (5 wt%) to form the catalyst ink. Then, 3.0 μl of this ink was dropped on GC electrode and dried naturally to from working electrode.

## 3 Results and discussion

### 3.1 Synthesis and structural characterization of Pd/GO-MXene-PS

The fabrication processes of Pd/GO-MXene-PS are illustrated in Scheme 1, which involves the following steps: (1) Etching of $Ti_3C_2T_x$ nanosheets; (2) GO was obtained by the improved Hummer method; (3) Synthesis of PS spheres by a slightly modified microemulsion polymerization strategy without surfactant; (4) Pd/GO-MXene-PS catalyst was got by condensation reflux at 120 °C, followed by calcination at 500 °C.

The composition and surface morphology of the material were analyzed by SEM, TEM and HRTEM. As can be seen from Fig. 1a, b, the 3D porous interconnect structure was successfully fabricated. Surprisingly, $Ti_3C_2T_x$ nanosheets and graphene nanosheets were stacked on each other to form a 3D network, which successfully prevented their reassembling or stacking in a hybrid system. In Fig. S2a, b, EDS results reveal that C, O, Ti and Pd elements co-existed in the three-dimensional porous structure. Furthermore, after reduction, Pd nanoparticles (NPs) can be

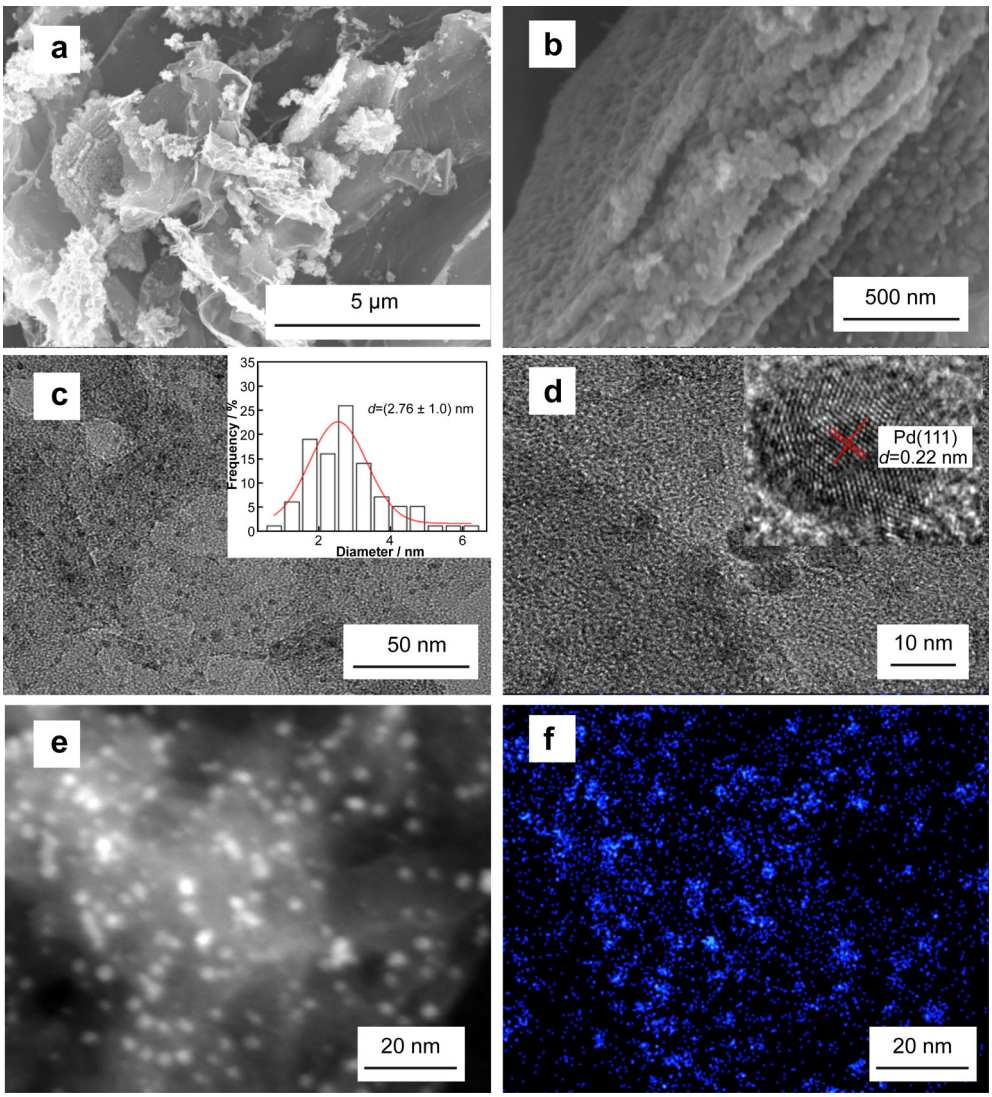


**Fig. 1** **a**, **b** SEM images of Pd/GO-MXene-PS; **c**, **d** TEM images of Pd/$GO_5$-$MXene_5$-PS; **e** HRTEM image of Pd/$GO_5$-$MXene_5$-PS; **f** elemental mapping of Pd

uniformly distributed on the carbon-based carrier. The loading of Pd in the prepared catalyst (range from 15.3 to 18.4 wt%) by ICP-OES is summarized in Table S1. Under closer inspection of Fig. 1c, d, the porous structure produced by the calcination of PS can be observed. Figure 1c, d also depicts that Pd nanoparticles are evenly distributed on regular porous carriers, and the size of Pd nanoparticles is rather small of (2.76 ± 1.0) nm. This is mainly attributed to the unique 3D porous structure of the catalyst. Meanwhile, it is related to the abundant functional groups (e.g., −OH, −F and −COOH) on the template material. These functional groups provide more active sites for the Pd NPs, which facilitate the adequate dispersion and particle size reduction in Pd NPs. The 3D structure can greatly accelerate the electron transmission rate and enhance the conductivity of the material [33]. HRTEM image demonstrates the crystalline of Pd nanoparticles and the measured lattice spacing of 0.21 nm for the (111) crystal plane of Pd nanoparticles (inset of Fig. 1d) [34]. This result can be confirmed with the followed XRD results. In addition, from HRTEM image in Fig. 1e and the corresponding Pd element mapping Fig. 1f, it can be seen that Pd nanoparticles are uniformly distributed on the composite support, which is also mutually verified with the previous results.

XRD analysis is generally used to distinguish the composition of species in the catalyst. As illustrated in Fig. 2a, the diffraction peak around 23.8° corresponds to the (002) crystal plane of carbon, indicating that GO and MXene are fully combined during the ultrasonic process [35]. The diffraction peaks of all synthetic materials near 40°, 44.12° and 67.62° could ascribe to the (111), (200) and (220)

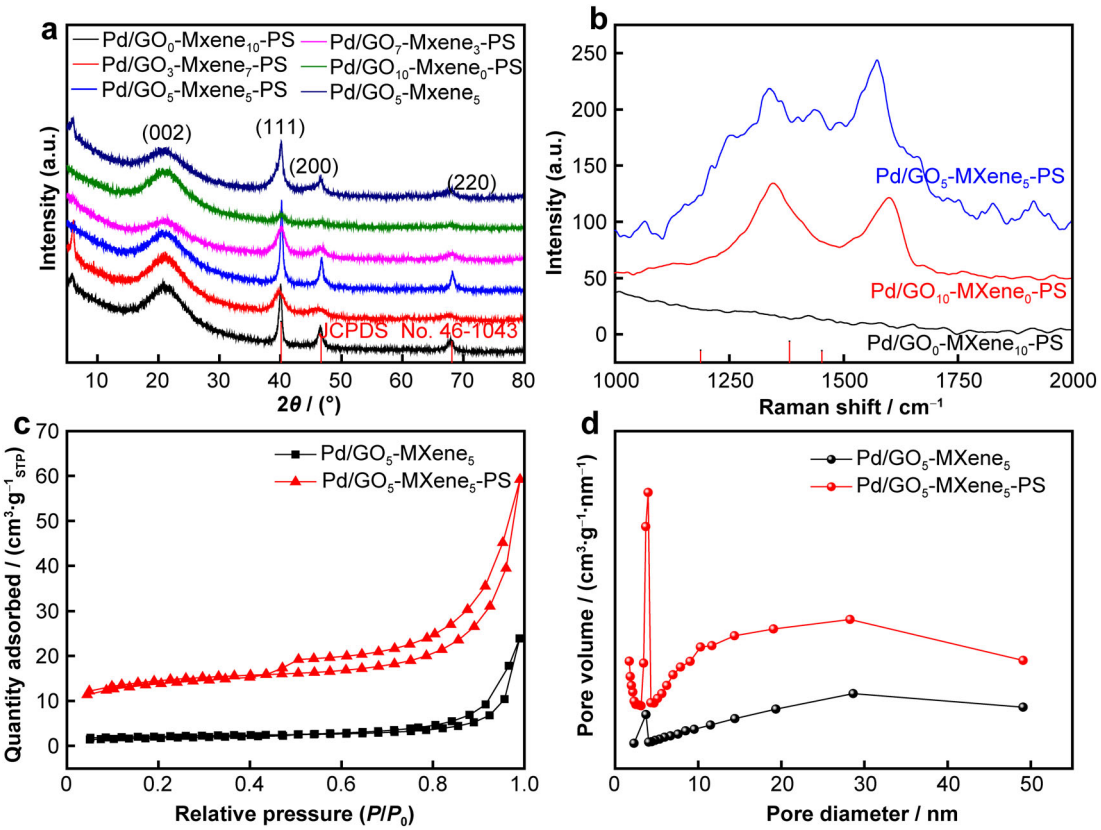


**Fig. 2** **a** XRD patterns of Pd/$GO_{10}$-$MXene_0$-PS, Pd/$GO_7$-$MXene_3$-PS, Pd/$GO_5$-$MXene_5$-PS, Pd/$GO_3$-$MXene_7$-PS, Pd/$GO_0$-$MXene_{10}$-PS and Pd/$GO_5$-$MXene_5$; **b** Raman spectra of Pd/$GO_{10}$-$MXene_0$-PS, Pd/$GO_5$-$MXene_5$-PS and Pd/$GO_0$-$MXene_{10}$-PS; **c** $N_2$ adsorption/desorption isotherms of Pd/$GO_5$-$MXene_5$-PS and Pd/$GO_5$-$MXene_5$; **d** pore size distribution of Pd/$GO_5$-$MXene_5$-PS and Pd/$GO_5$-$MXene_5$

crystal of Pd element, which also confirms the face-centered cubic crystal structure of Pd element (JCPDS No. 46-1043) [36]. On the other hand, this also means a good dispersion of Pd NPs on GO-MXene-PS composites. The crystallite size calculated from Debye–Scherrer equation [13] is in the following order: Pd/$GO_5$-$MXene_5$ > Pd/$GO_{10}$-$MXene_0$-PS > Pd/$GO_0$-$MXene_{10}$-PS > Pd/$GO_7$-$MXene_3$-PS > Pd/$GO_3$-$MXene_7$-PS > Pd/$GO_5$-$MXene_5$-PS, as shown in Table 1. It can be found that the PS-treated catalyst has a smaller particle size, mainly because PS-treated catalyst has a unique three-dimensional porous structure and abundant anchor groups (such as −OH, −F and −COOH) on the surface. This is not conducive to the formation of large Pd clusters or aggregates on the catalyst surface. As indicated in Fig. 2b, the Raman spectra of Pd/$GO_5$-$MXene_5$-PS provide two distinct peaks centered at 1590 $cm^{-1}$ (G band) and 1339 $cm^{-1}$ (D band) which correspond to the feature bands of graphene [37–40]. These results also reveal that GO is fully combined with MXene and can be mutually confirmed with XRD results. Nitrogen adsorption–desorption isotherms and pore size distribution of three kinds of supports verified the typical type IV isotherms (Fig. 2c, d) suggesting the presence of

**Table 1** Crystallite size and peak position of Pd/GO-MXene-PS catalysts on Pd (111) crystal plane

| Catalysts | 2$\theta$ position / (°) | Crystallite size / nm |
|---|---|---|
| Pd/$GO_{10}$-$MXene_0$-PS | 40.33 | 5.6 |
| Pd/$GO_7$-$MXene_3$-PS | 40.32 | 4.3 |
| Pd/$GO_5$-$MXene_5$-PS | 40.20 | 3.7 |
| Pd/$GO_3$-$MXene_7$-PS | 39.86 | 4.2 |
| Pd/$GO_0$-$MXene_{10}$-PS | 40.02 | 5.4 |
| Pd/$GO_5$-$MXene_5$ | 40.14 | 7.1 |

mesopores and macropores structures [41, 42]. The BET surface area of Pd/$GO_5$-$MXene_5$-PS is 46.74 $m^2g^{-1}$, outperforming that of the pristine Pd/$GO_5$-$MXene_5$ (6.94 $m^2g^{-1}$). Using PS as a sacrificial template can significantly increase the specific surface area, which implies that the Pd/$GO_5$-$MXene_5$-PS catalyst may provide more active sites for contact with metal ions.

XPS measurements are further conducted to probe the elemental valence states of the Pd/$GO_5$-$MXene_5$-PS architecture. As can be seen from Fig. 3a, Pd/$GO_5$-$MXene_5$-PS mainly includes six elements: Pd 3d, F 1s,

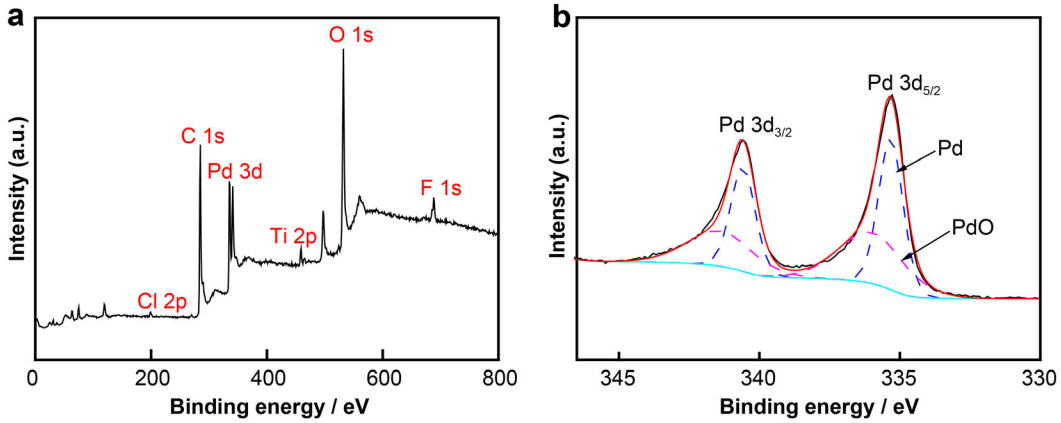


**Fig. 3** XPS spectra of Pd/$GO_5$-$MXene_5$-PS: **a** survey spectrum, **b** high-resolution spectrum of Pd 3d

Cl 2p, Ti 2p, O 1s and C 1s. From Fig. 3b, Pd 3d in Pd/$GO_5$-$MXene_5$-PS contains two characteristic peaks, Pd $3d_{5/2}$ and Pd $3d_{3/2}$ [43]. Pd 3d spectra were divided into two peaks, indicating that the elemental Pd and Pd oxide (PdO) coexist in the catalyst. Among them, two strong peaks located at 335.1 and 340.4 eV are attributed to $Pd^0$, the other two relatively weak peaks (336.5 and 342.1 eV) are ascribed to Pd oxide [44]. The peaks of Pd nanoparticles in the Pd/$GO_5$-$MXene_5$-PS composite are mainly elemental Pd, which is beneficial to the catalytic oxidation of ethanol.

## 3.2 Electrochemical measurements

As reported in Fig. 4a, the stable CV curves of commercial Pd/C and the as-prepared catalysts range from − 0.25 to 1.2 V (*j* stands for current density, *E* stands for scanning potential). The PdO reduction peak potentials of the prepared catalysts were all about 0.4 V. Electrochemical active surface area (ECSA) [45] values of Pd/C, Pd/$GO_{10}$-$MXene_0$-PS, Pd/$GO_7$-$MXene_3$-PS, Pd/$GO_5$-$MXene_5$-PS, Pd/$GO_3$-$MXene_7$-PS, Pd/$GO_0$-$MXene_{10}$-PS and Pd/$GO_5$-

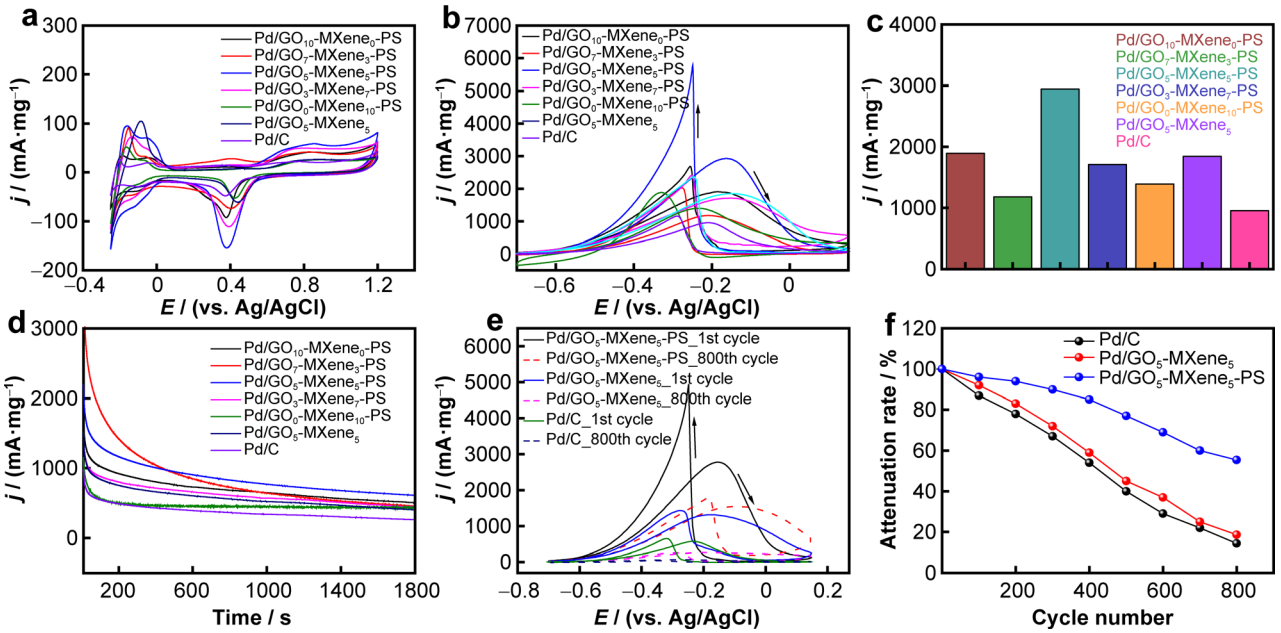


**Fig. 4** CV curves of Pd/$GO_{10}$-$MXene_0$-PS, Pd/$GO_7$-$MXene_3$-PS, Pd/$GO_5$-$MXene_5$-PS, Pd/$GO_3$-$MXene_7$-PS, Pd/$GO_0$-$MXene_{10}$-PS, Pd/$GO_5$-$MXene_5$ and commercial Pd/C in **a** 0.5 mol·$L^{-1}$ $H_2SO_4$; **b** 1 mol·$L^{-1}$ KOH + 1 mol·$L^{-1}$ $C_2H_5OH$; **c** mass activities **d** *j*-*t* curves in 1 mol·$L^{-1}$ KOH + 1 mol·$L^{-1}$ $C_2H_5OH$; **e** CVs of Pd/$GO_5$-$MXene_5$-PS, Pd/$GO_5$-$MXene_5$ and commercial Pd/C catalysts before and after 800 potential cycles; **f** EOR durability comparison of Pd/$GO_5$-$MXene_5$-PS, Pd/$GO_5$-$MXene_5$ and Pd/C in 1 mol·$L^{-1}$ KOH + 1 mol·$L^{-1}$ $C_2H_5OH$

**Table 2** Initial oxidation potential, peak potential, peak current and ECSA from evaluation of EOR of electrocatalysts in 1 mol·L$^{-1}$ KOH + 1 mol·L$^{-1}$ $C_2H_5OH$

| Samples | Initial oxidation potential / V | Forward oxidation peak potential / V | Forward oxidation peak current / (mA·mg$^{-1}$) | ECSA / (m$^2$·g$^{-1}$) |
|---|---|---|---|---|
| Pd/$GO_{10}$-$MXene_0$-PS | − 0.58 | − 0.18 | 1892.9 | 54.5 |
| Pd/$GO_7$-$MXene_3$-PS | − 0.55 | − 0.20 | 1177.3 | 60.7 |
| Pd/$GO_5$-$MXene_5$-PS | − 0.54 | − 0.15 | 2944.0 | 89.9 |
| Pd/$GO_3$-$MXene_7$-PS | − 0.56 | − 0.15 | 1707.0 | 52.2 |
| Pd/$GO_0MXene_{10}$-PS | − 0.61 | − 0.23 | 1390.7 | 17.5 |
| Pd/$GO_5$-$MXene_5$ | − 0.59 | − 0.14 | 1844.4 | 58.7 |
| Pd/C | − 0.55 | − 0.21 | 950.4 | 12.3 |

$MXene_5$ are presented in Table 2. ECSA values of Pd/$GO_{10}$-$MXene_0$-PS, Pd/$GO_7$-$MXene_3$-PS, Pd/$GO_5$-$MXene_5$-PS, Pd/$GO_3$-$MXene_7$-PS, Pd/$GO_0$-$MXene_{10}$-PS and Pd/$GO_5$-$MXene_5$ were higher than that of commercial Pd/C catalyst, and Pd/$GO_5$-$MXene_5$-PS catalyst had the highest ECSA value. This indicates that under the condition of GO: MXene is equal to 5:5, ECSA of PS sphere hybrid material is larger than that of the material without PS hybridization. In Fig. 4b, c, Pd/$GO_{10}$-$MXene_0$-PS, Pd/$GO_7$-$MXene_3$-PS, Pd/$GO_5$-$MXene_5$-PS, Pd/$GO_3$-$MXene_7$-PS, Pd/$GO_0$-$MXene_{10}$-PS and Pd/$GO_5$-$MXene_5$ postulate better electrooxidation performance of ethanol than that of commercial Pd/C. Pd/$GO_5$-$MXene_5$-PS catalyst possesses the highest mass activity (2944.0 mA·mg$^{-1}$), which was 3.0, 1.5, 2.5, 1.7, 2.1 and 1.5 times of the current densities of commercial Pd/C(950.4 mA·mg$^{-1}$), Pd/$GO_{10}$-$MXene_0$-PS (1892.9 mA·mg$^{-1}$), Pd/$GO_7$-$MXene_3$-PS (1177.3 mA·mg$^{-1}$), Pd/$GO_3$-$MXene_7$-PS (1707.0 mA·mg$^{-1}$), Pd/$GO_0$-$MXene_{10}$-PS (1390.7 mA·mg$^{-1}$) and Pd/$GO_5$-$MXene_5$ (1844.4 mA·mg$^{-1}$), respectively. In addition, the stability of the electrocatalysts is assessed by chronoamperometry (Fig. 4d). Pd/$GO_{10}$-$MXene_0$-PS, Pd/$GO_7$-$MXene_3$-PS, Pd/$GO_5$-$MXene_5$-PS, Pd/$GO_3$-$MXene_7$-PS, Pd/$GO_0$-$MXene_{10}$-PS and Pd/$GO_5$-$MXene_5$ catalysts illustrate higher stability than that of the commercial Pd/C, and the Pd/$GO_5$-$MXene_5$-PS catalyst has the best stability among them. Table 3 evaluates the electrochemical performance of different Pd-based catalysts and compares their catalytic activities with the literature, and Pd/$GO_5$-$MXene_5$-PS material has excellent catalytic ethanol oxidation performance. As shown in Fig. 4e, f, the current densities of Pd/$GO_5$-$MXene_5$-PS, Pd/$GO_5$-$MXene_5$ and commercial Pd/C catalysts provided a slow decreasing trend with increasing CV cycle number. After 800 CV cycling, the initial catalytic activity of Pd/$GO_5$-$MXene_5$-PS is 55.4%, which is significantly better than that of Pd/$GO_5$-$MXene_5$ (18.6%) and commercial Pd/C (14.4%). Even at time of 1800 s, the current density of Pd/$GO_5$-$MXene_5$-PS is still much higher than that of Pd/$GO_5$-$MXene_5$ and commercial Pd/C. These results further indicate the high electrochemical durability of Pd/$GO_5$-$MXene_5$-PS. The enhanced kinetic activity of Pd/GO-MXene-PS mainly attributed to optimization of support structure. Among them, MXene provides more abundant functional groups, which provide more active sites for Pd NPs. Graphene prevents the aggregation between MXene lamellae and accelerates the ion transport between the lamellae, thus improving the catalytic performance.

**Table 3** Comparison of Pd-based catalysts for ethanol oxidation in literatures

| Catalysts | Electrolytes | Mass activity / (mA·mg$^{-1}$) | ECSA / (m$^2$·g$^{-1}$) | Refs. |
|---|---|---|---|---|
| Pd/$Ni(OH)_2$/C | 0.1 mol·L$^{-1}$ KOH + 0.5 mol·L$^{-1}$ $C_2H_5OH$ | 2532.7 | – | [51] |
| Pd/$Ni(OH)_2$/Ni foam | 1.0 mol·L$^{-1}$ KOH + 1.0 mol·L$^{-1}$ $C_2H_5OH$ | 1295.0 | – | [52] |
| PdNi/ERPGO | 1.0 mol·L$^{-1}$ KOH + 1.0 mol·L$^{-1}$ $C_2H_5OH$ | 1546.0 | – | [53] |
| Ni@Pd/MWCNT | 1.0 mol·L$^{-1}$ KOH + 1.0 mol·L$^{-1}$ $C_2H_5OH$ | 3495.0 | – | [54] |
| Pd/LHPC | 1.0 mol·L$^{-1}$ KOH + 1.0 mol·L$^{-1}$ $C_2H_5OH$ | 2096.3 | 12.5 | [55] |
| Pd/AG-$Ni_3N$ | 1.0 mol·L$^{-1}$ NaOH + 1.0 mol·L$^{-1}$ $C_2H_5OH$ | 3499.5 | 149.3 | [56] |
| $Pt_{36}Pd_{41}Cu_{23}$NWs | 0.5 mol·L$^{-1}$ $H_2SO_4$ + 1.0 mol·L$^{-1}$ $C_2H_5OH$ | 1856.0 | 43.0 | [57] |
| PtCo-NC | 0.5 mol·L$^{-1}$ $H_2SO_4$ + 1.0 mol·L$^{-1}$ $C_2H_5OH$ | 438.8 | 55.0 | [58] |
| Pd/PtFe NTs | 0.1 mol·L$^{-1}$ $HClO_4$ + 0.5 mol·L$^{-1}$ $C_2H_5OH$ | 2340.0 | 62.7 | [59] |
| Pd/$GO_5$-$MXene_5$-PS | 1.0 mol·L$^{-1}$ KOH + 1.0 mol·L$^{-1}$ $C_2H_5OH$ | 2944.0 | 89.9 | This work |

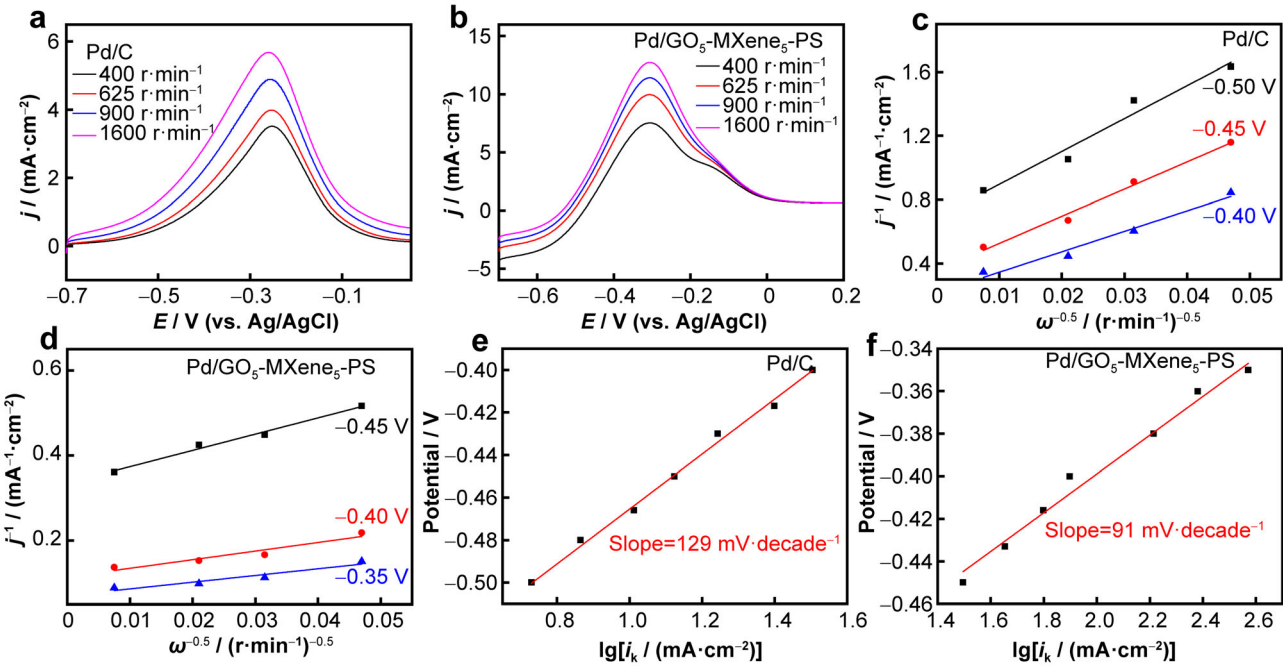


**Fig. 5** RDE testing of **a** commercial Pd/C and **b** Pd/$GO_5$-$MXene_5$-PS at different RDE rotation rates in 1.0 mol·$L^{-1}$ methanol + 1.0 mol·$L^{-1}$ KOH at 20 mV·$s^{-1}$; Koutecky-Levich plots for EOR of **c** commercial Pd/C and **d** Pd/$GO_5$-$MXene_5$-PS; Tafel slopes of **e** commercial Pd/C and **f** Pd/$GO_5$-$MXene_5$-PS

Here, we used RDE to determine the effect of different rotational speeds on the ethanol oxidation current by varying the rotational speed (Fig. 5a, b). $\omega$ and $i_k$ represent rotate speed and current per unit area, respectively. The results showed that the ethanol oxidation current values of both catalysts tended to increase with the increase in the rotational speed. On the other hand, we investigate the effect of different scan rates on the oxidation current of ethanol and the results remain consistent with the above (Fig. S3a, b). A smooth straight line can be observed in the inset of Fig. S3a, b, respectively. Therefore, it can be concluded that there is a clear linear relationship implying the EOR process is a diffusion control process [46]. Figure 5c, d shows the fitted curves of the two catalysts after the Koutecky–Levich equation calculation [47]. Since the fitted curves are smooth straight lines, it can also be proved that the ethanol oxidation process is a fully diffusion-controlled process [48]. In general, the smaller the Tafel slope, the greater the kinetic rate of the reaction [49, 50]. From Fig. 5e, f, the Tafel slope of Pd/$GO_5$-$MXene_5$-PS (91 mV·$decade^{-1}$) is smaller than that of commercial Pd/C (129 mV·$decade^{-1}$), implying that Pd/$GO_5$-$MXene_5$-PS possesses a faster ethanol oxidation kinetics. This is mainly due to the fact that MXene and graphene overlap each other, which reduces the electron transfer distance and increases the electron transfer rate. Figure S4 shows the electrochemical impedance spectroscopy (EIS) of commercial Pd/C and Pd/$GO_5$-$MXene_5$-PS. From Fig. S4, it can be found that the semicircle radius of Pd/$GO_5$-$MXene_5$-PS is smaller than that of commercial Pd/C. This result indicates that Pd/$GO_5$-$MXene_5$-PS has a lower charge transfer resistance and the better conductivity, which is favorable to accelerate the kinetics of ethanol oxidation.

## 4 Conclusion

In summary, we successfully prepared a 3D layered structure of Pd/GO-MXene-PS by one-step synthesis strategy. By sacrificing PS as the template material, it assists to produce a three-dimensional interconnected structure that supports ion and electron transport. By optimizing the doping ratio of MXene to GO, the mass activity of Pd/$GO_5$-$MXene_5$-PS (2944.0 mA·$mg^{-1}$) is 3.0 times higher than that of commercial Pd/C (950.4 mA·$mg^{-1}$). RDE results further demonstrate that the Tafel slope of Pd/$GO_5$-$MXene_5$-PS (91 mV·$decade^{-1}$) is smaller than that of commercial Pd/C (129 mV·$decade^{-1}$), implying that Pd/$GO_5$-$MXene_5$-PS possesses a faster ethanol oxidation kinetic. The enhanced mass activity, faster mass transport and kinetic process of ethanol oxidation of Pd/$GO_5$-$MXene_5$-PS can attribute to the excellent 3D interconnected porous structure, large surface area, good conductivity and homogeneous Pd distribution. This experiment proposes an approach for

preparing 3D MXene composite materials which provides a new direction for the development of Pd-based catalysts for DEFC.

**Acknowledgements** This study was financially supported by the Program for Professor of Special Appointment (Eastern Scholar) at Shanghai Institutions of Higher Learning (No. A30B191410), the Sailing Project from Science and Technology Commission of Shanghai Municipality (No. 17YF1406600), Chenguang Project Supported by Shanghai Municipal Education Commission (No. 18CG68) and Gaoyuan Discipline of Shanghai-Materials Science and Engineering (No. A30NH221903), the Open Project of Jiangsu Key Laboratory for Carbon-Based Functional Materials & Devices (Soochow University) (No. KS2022), Collaborative Innovation Center of Suzhou Nano Science & Technology, the 111 Project, Joint International Research Laboratory of Carbon-Based Functional Materials and Devices, and the Project of Guangdong Provincial Education (No. 2020KTSCX131).

### Declarations

**Conflict of interests** The authors declare that they have no conflict of interest.

## References

[1] Dorner RW, Hardy DR, Williams FW, Willauer HD. Heterogeneous catalytic $CO_2$ conversion to value-added hydrocarbons. Energy Environ Sci. 2010;3(7):884.
[2] Cui MS, Zhang YQ, Zhong Q, Long ZQ, Zhao N, Huang XW. Portable XRF analysis of noble metal contents for automotive catalysts. Chinese J Rare Met. 2020;44(11):1227.
[3] Akhairi MAF, Kamarudin SK. Catalysts in direct ethanol fuel cell (DEFC): an overview. Int J Hydrogen Energy. 2016;41(7):4214.
[4] Chen A, Ostrom C. Palladium-based nanomaterials: synthesis and electrochemical applications. Chem Rev. 2015;115(21):11999.
[5] Zhang Y, Yuan X, Lyu FL, Wang XC, Jiang XJ, Cao MH, Zhang Q. Facile one-step synthesis of PdPb nanochains for high-performance electrocatalytic ethanol oxidation. Rare Met. 2020;39(7):792.
[6] Sheng T, Qiu C, Lin X, Lin WF, Sun SG. Insights into ethanol electro-oxidation over solvated Pt(100): origin of selectivity and kinetics revealed by DFT. Appl Surf Sci. 2020;533: 147505.
[7] Maya-Cornejo J, Diaz-Real JA, Lopez-Miranda JL, Álvarez-Contreras L, Esparza R, Arjona N, Estévez M. Formation of Cu@Pd core@shell nanocatalysts with high activity for ethanol electro-oxidation in alkaline medium. Appl Surf Sci. 2021. https://doi.org/10.1016/j.apsusc.2020.148119.
[8] Shafaei Douk A, Saravani H, Noroozifar M. Novel fabrication of PdCu nanostructures decorated on graphene as excellent electrocatalyst toward ethanol oxidation. Int J Hydrogen Energy. 2017;42(22):15149.
[9] Zhang Y, Liu Q, Shao X, Ma W, Feng YN. Progress in fabrication and application of graphene nanoribbons. Chinese J Rare Met. 2021;45(9):1119.
[10] Taei M, Havakeshian E, Salavati H, Azemati M. Highly active electrocatalysts for ethanol oxidation based on gold nanodendrites modified with $NiFe_2O_4$ nanoparticles decorated multi-walled carbon nanotubes. Chem Pap. 2019;73(11):2687.
[11] Young SJ, Lin ZD. Ethanol gas sensors based on multi-wall carbon nanotubes on oxidized Si substrate. Microsyst Technol. 2016;24(1):55.
[12] Sudachom N, Warakulwit C, Prapainainar C, Witoon T, Prapainainar P. One step $NaBH_4$ reduction of Pt-Ru-Ni catalysts on different types of carbon supports for direct ethanol fuel cells: synthesis and characterization. J Fuel Chem Technol. 2017;45(5):596.
[13] Lin D, Jiang Y, Chen S, Chen S, Sun S. Preparation of Pt nanoparticles supported on ordered mesoporous carbon FDU-15 for electrocatalytic oxidation of CO and methanol. Electrochim Acta. 2012;67:127.
[14] Geng D, Zhu S, Chai M, Zhang Z, Fan J, Xu Q, Min Y. $Pd_xFe_y$ alloy nanoparticles decorated on carbon nanofibers with improved electrocatalytic activity for ethanol electrooxidation in alkaline media. New J Chem. 2020;44(13):5023.
[15] Carrión-Satorre S, Montiel M, Escudero-Cid R, Fierro JLG, Fatás E, Ocón P. Performance of carbon-supported palladium and palladium ruthenium catalysts for alkaline membrane direct ethanol fuel cells. Int J Hydrogen Energy. 2016;41(21):8954.
[16] Ramli ZAC, Kamarudin SK. Platinum-based catalysts on various carbon supports and conducting polymers for direct methanol fuel cell applications: a review. Nanoscale Res Lett. 2018;13(1):410.
[17] Xiu L, Wang Z, Yu M, Wu X, Qiu J. Aggregation-resistant 3D MXene-based architecture as efficient bifunctional electrocatalyst for overall water splitting. ACS Nano. 2018;12(8):8017.
[18] Qiu ZM, Bai Y, Gao YD, Liu CL, Ru Y, Pi YC, Zhang YZ, Luo YS, Pang H. MXenes nanocomposites for energy storage and conversion. Rare Met. 2021. https://doi.org/10.1007/s12598-021-01876-0.
[19] Kshetri T, Tran DT, Le HT, Nguyen DC, Hoa HV, Kim NH, Lee JH. Recent advances in MXene-based nanocomposites for electrochemical energy storage applications. Prog Mater Sci. 2021;117: 100733.
[20] Xiu LY, Wang ZY, Qiu JS. General synthesis of MXene by green etching chemistry of fluoride-free Lewis acidic melts. Rare Met. 2020;39(11):1237.
[21] Xiao W, Yan D, Zhang Y, Yang X, Zhang T. Heterostructured $MoSe_2$/oxygen-terminated $Ti_3C_2$ MXene architectures for efficient electrocatalytic hydrogen evolution. Energy Fuels. 2021;35(5):4609.
[22] Maiti UN, Lim J, Lee KE, Lee WJ, Kim SO. Three-dimensional shape engineered, interfacial gelation of reduced graphene oxide for high rate, large capacity supercapacitors. Adv Mater. 2014;26(4):615.
[23] Boota M, Anasori B, Voigt C, Zhao MQ, Barsoum MW, Gogotsi Y. Pseudocapacitive electrodes produced by oxidant-free polymerization of pyrrole between the layers of 2D titanium carbide (MXene). Adv Mater. 2016;26(4):615.
[24] Zhao MQ, Ren CE, Ling Z, Lukatskaya MR, Zhang C, Van Aken KL, Barsoum MW, Gogotsi Y. Flexible MXene/carbon nanotube composite paper with high volumetric capacitance. Adv Mater. 2016;28(7):1517.
[25] Yi QF, Sun LZ. In situ synthesis of palladium nanoparticles on multi-walled carbon nanotubes and their electroactivity for ethanol oxidation. Rare Met. 2013;32(6):586.
[26] Hren M, Hribernik S, Gorgieva S, Motealleh A, Eqtesadi S, Wendellbo R, Lue SJ, Božič M. Chitosan-$Mg(OH)_2$ based composite membrane containing nitrogen doped GO for direct ethanol fuel cell. Cellulose. 2021;28(3):1599.
[27] Zhang Q, Li Y, Chen T, Li L, Shi S, Jin C, Yang B, Hou S. Fabrication of 3D interconnected porous MXene-based PtNPs as highly efficient electrocatalysts for methanol oxidation. J Electroanal Chem. 2021;894: 115338.

[28] Zhao MQ, Torelli M, Ren CE, Ghidiu M, Ling Z, Anasori B, Barsoum MW, Gogotsi Y. 2D titanium carbide and transition metal oxides hybrid electrodes for Li-ion storage. Nano Energy. 2016;30:603.
[29] Yang C, Jiang Q, Li W, He H, Yang L, Lu Z, Huang H. Ultrafine Pt nanoparticle-decorated 3D hybrid architectures built from reduced graphene oxide and mxene nanosheets for methanol oxidation. Chem Mater. 2019;31(22):9277.
[30] Wu M, An Y, Yang R, Tao Z, Xia Q, Hu Q, Li M, Chen K, Zhang Z, Huang Q, Ma S, Zhou A. $V_2CT_x$ and $Ti_3C_2T_x$ MXenes nanosheets for gas sensing. ACS Appl Nano Mater. 2021;4(6):6257.
[31] Zhang C, Pansare VJ, Prud'homme RK, Priestley RD. Flash nanoprecipitation of polystyrene nanoparticles. Soft Matter. 2012;8(1):86.
[32] Yuan R, Yuan J, Wu Y, Ju P, Ji L, Li H, Chen L, Zhou H, Chen J. Graphene oxide-monohydrated manganese phosphate composites: preparation via modified Hummers method. Colloids Surf A. 2018;547:56.
[33] Yang W, Yang W, Song A, Sun G, Shao G. 3D interconnected porous carbon nanosheets/carbon nanotubes as a polysulfide reservoir for high performance lithium-sulfur batteries. Nanoscale. 2018;10(2):816.
[34] Alvarenga GM, Coutinho Gallo IB, Villullas HM. Enhancement of ethanol oxidation on Pd nanoparticles supported on carbon-antimony tin oxide hybrids unveils the relevance of electronic effects. J Catal. 2017;348:1.
[35] Promsawan N, Saipanya S, Rattanakansang S, Themsirimongkon S, Inceesungvorn B, Waenkaew P. Modification of various carbons with various metal oxides and noble metal compositions as electrocatalysts for ethanol oxidation. Compos Interfaces. 2020;27(11):1023.
[36] Zhang P, Fan C, Wang R, Xu C, Cheng J, Wang L, Lu Y, Luo P. Pd/MXene($Ti_3C_2T_x$)/reduced graphene oxide hybrid catalyst for methanol electrooxidation. Nanotechnology. 2020. https://doi.org/10.1088/1361-6528/ab5609.
[37] Huang H, Ye G, Yang S, Fei H, Tiwary CS, Gong Y, Vajtai R, Tour JM, Wang X, Ajayan PM. Nanosized Pt anchored onto 3D nitrogen-doped graphene nanoribbons towards efficient methanol electrooxidation. J Mater Chem A. 2015;3(39):19696.
[38] Li M, Jiang Q, Yan M, Wei Y, Zong J, Zhang J, Wu Y, Huang H. Three-dimensional boron- and nitrogen-codoped graphene aerogel-supported Pt nanoparticles as highly active electrocatalysts for methanol oxidation reaction. ACS Sustain Chem Eng. 2018;6(5):6644.
[39] Lu KC, Wang JK, Lin DH, Chen X, Yin SY, Chen GS. Construction of a novel electrochemical biosensor based on a mesoporous silica/oriented graphene oxide planar electrode for detecting hydrogen peroxide. Anal Methods. 2020;12(21):2661.
[40] Chen X, Lu K, Lin D, Li Y, Yin S, Zhang Z, Tang M, Chen G. Hierarchical porous tubular biochar based sensor for detection of trace lead (II). Electroanalysis. 2021;33:473.
[41] Lin D, Zhang X, Cui X, Chen W. Highly porous carbons with superior performance for $CO_2$ capture through hydrogen-bonding interactions. RSC Adv. 2014;4(52):27414.
[42] Zhang X, Lin D, Chen W. Nitrogen-doped porous carbon prepared from a liquid carbon precursor for $CO_2$ adsorption. RSC Adv. 2015;5(56):45136.
[43] Scheibe B, Tadyszak K, Jarek M, Michalak N, Kempiński M, Lewandowski M, Peplińska B, Chybczyńska K. Study on the magnetic properties of differently functionalized multilayered $Ti_3C_2T_x$ MXenes and Ti-Al-C carbides. Appl Surf Sci. 2019;479:216.
[44] Yao C, Zhang Q, Su Y, Xu L, Wang H, Liu J, Hou S. Palladium nanoparticles encapsulated into hollow N-doped graphene microspheres as electrocatalyst for ethanol oxidation reaction. ACS Appl Nano Mater. 2019;2(4):1898.
[45] Yu X, Liu J, Li J, Luo Z, Zuo Y, Xing C, Llorca J, Nasiou D, Arbiol J, Pan K, Kleinhanns T, Xie Y, Cabot A. Phosphorous incorporation in $Pd_2Sn$ alloys for electrocatalytic ethanol oxidation. Nano Energy. 2020;77:105116.
[46] Kurt Urhan B, Öztürk Doğan H, Çepni E, Eryiğit M, Demir Ü, Öznülüer ÖT. $Ni(OH)_2$-electrochemically reduced graphene oxide nanocomposites as anode electrocatalyst for direct ethanol fuel cell in alkaline media. Chem Phys Lett. 2021;763: 138208.
[47] Hou G, Parrondo J, Ramani V, Prakash J. Kinetic and mechanistic investigation of methanol oxidation on a smooth polycrystalline Pt surface. J Electrochem Soc. 2013;161(3):F252.
[48] Yousaf AB, Imran M, Uwitonze N, Zeb A, Zaidi SJ, Ansari TM, Yasmeen G, Manzoor S. Enhanced electrocatalytic performance of $pt_3pd_1$ alloys supported on $CeO_2$/C for methanol oxidation and oxygen reduction reactions. J Phys Chem C. 2017;121(4):2069.
[49] Liu H, Yang D, Bao Y, Yu X, Feng L. One-step efficiently coupling ultrafine Pt–$Ni_2P$ nanoparticles as robust catalysts for methanol and ethanol electro-oxidation in fuel cells reaction. J Power Sour. 2019;434: 226754.
[50] Chen Y, Ma Y, Zhou Y, Huang Y, Li S, Chen Y, Wang R, Tang J, Wu P, Zhao X, Chen C, Zhu Z, Chen S, Cheng K, Lin D. Enhanced methanol oxidation on PtNi nanoparticles supported on silane-modified reduced graphene oxide. Int J Hydrogen Energy. 2022;47(10):6638.
[51] Zhong J, Bin D, Yan B, Feng Y, Zhang K, Wang J, Wang C, Shiraishi Y, Yang P, Du Y. Highly active and durable flowerlike Pd/$Ni(OH)_2$ catalyst for the electrooxidation of ethanol in alkaline medium. RSC Adv. 2016;6(76):72722.
[52] Li C, Wen H, Tang PP, Wen XP, Wu LS, Dai HB, Wang P. Effects of $Ni(OH)_2$ morphology on the catalytic performance of Pd/$Ni(OH)_2$/Ni foam hybrid catalyst toward ethanol electrooxidation. ACS Appl Energy Mater. 2018;1(11):6040.
[53] Huang W, Ma XY, Wang H, Feng R, Zhou J, Duchesne PN, Zhang P, Chen F, Han N, Zhao F, Zhou J, Cai WB, Li Y. Promoting effect of $Ni(OH)_2$ on palladium nanocrystals leads to greatly improved operation durability for electrocatalytic ethanol oxidation in alkaline solution. Adv Mater. 2017;29(37):1703057.
[54] Zhang M, Yan Z, Xie J. Core/shell Ni@Pd nanoparticles supported on MWCNTs at improved electrocatalytic performance for alcohol oxidation in alkaline media. Electrochim Acta. 2012;77:237.
[55] Xu H, Qing Y, Xiong F, Wu Y. Lignin-derived hierarchical porous carbon supported Pd nanoparticles as an efficient electrocatalyst for ethanol oxidation. J Porous Mater. 2020;28(2):337.
[56] Wu T, Wang X, Emrehan Emre A, Fan J, Min Y, Xu Q, Sun S. Graphene-nickel nitride hybrids supporting palladium nanoparticles for enhanced ethanol electrooxidation. J Energy Chem. 2021;55:48.
[57] Wang K, Wang F, Zhao Y, Zhang W. Surface-tailored PtPdCu ultrathin nanowires as advanced electrocatalysts for ethanol oxidation and oxygen reduction reaction in direct ethanol fuel cell. J Energy Chem. 2021;52:251.
[58] Fang B, Feng L. PtCo-NC catalyst derived from the pyrolysis of Pt-incorporated ZIF-67 for alcohols fuel electrooxidation. Acta Phys Chim Sin. 2020;36(7):1905023.
[59] Tao L, Xia Z, Zhang Q, Sun Y, Li M, Yin K, Gu L, Guo S. Spiny Pd/PtFe core/shell nanotubes with rich high-index facets for efficient electrocatalysis. Science Bulletin. 2021;66(1):44.